Residual stresses in surgical growing rods

Maïté Croonenborghs
Institute of Mechanics, Materials and Civil Engineering,
Université catholique de Louvain,
Place Sainte Barbe 2 L5.02.02,
1348 Louvain-la-Neuve, Belgium

Karim Ismail
Institute of Mechanics, Materials and Civil Engineering,
Université catholique de Louvain,
Place Sainte Barbe 2 L5.02.02,
1348 Louvain-la-Neuve, Belgium

Maryline Mousny
Centre Plurisanté,
11 avenue de l'Andalousie,
1140, Bruxelles, Belgium

Laurent Delannay
Institute of Mechanics, Materials and Civil Engineering,
Université catholique de Louvain,
Place Sainte Barbe 2 L5.02.02,
1348 Louvain-la-Neuve, Belgium

Joris Everaerts
Department of Materials Engineering,
KU Leuven,
Kasteelpark Arenberg 44 box 2450,
Leuven 3001, Belgium

Alexander M. Korsunsky
Department of Engineering Science,
University of Oxford,
Parks Road,
Oxford OX1 3PJ, United Kingdom

Pascal J. Jacques
Institute of Mechanics, Materials and Civil Engineering,
Université catholique de Louvain,
Place Sainte Barbe 2 L5.02.02,
1348 Louvain-la-Neuve, Belgium

Thomas Pardoen[1]
Institute of Mechanics, Materials and Civil Engineering,
Université catholique de Louvain,
Place Sainte Barbe 2 L5.02.02,
1348 Louvain-la-Neuve, Belgium

ABSTRACT

The treatment of early-onset scoliosis using surgical growing rods suffers from high failure rate. Fatigue resistance can be improved by inducing compressive residual stresses within the near surface region. An in-depth investigation of the residual stresses profile evolution is performed through the sequence of material processing steps followed by surgeons handling operations, in connection to material properties. The final goal is to guide further improvements of growing rod lifetime. Residual stress evaluation was carried out on Ti6Al4V rods using digital image correlation applied to micro-beam ring-core milling by focused ion beam. This provided experimental stress profiles in shot-peened rods before and after bending and demonstrated that compressive residual stresses are maintained at both concave and convex rod sides. A finite element model using different core and skin conditions was validated by comparison to experiments. The combination of an initial shot peening profile associated to a significant level of backstress was found to primarily control the generation of compressive stresses at the rod surface after bending. Guidelines to promote larger compressive stresses at the surface were formulated based on a parametric analysis. The analysis revealed the first order impact of the initial yield strength, kinematic hardening parameters and intensity of the shot peening operation, while the bending angle and the depth of shot peening stresses were found to be of minor importance. Materials exhibiting large kinematic hardening and low yield strength should be selected in order to induce compressive residual stresses at key fatigue initiation location.

[1] Corresponding author: thomas.pardoen@uclouvain.be Tel.: +32 10 / 47 24 17

1. CONTEXT

When children suffer from severe scoliosis pathology, fusion-type surgery is not acceptable due to the severe impact on the growth of the spine. Among others, proper lung development is closely related to adequate spine growth [1]. As spinal fusion method is not suited for immature skeletons, other corrective techniques have to be used [2,3]. The decision about the alternative option is made based on the patient profile. Among these alternative techniques, the implantation of growing rods is widely used throughout the world.

The growing rod strategy consists in one or multiple long cylindrical rods inserted in the back to correct for spurious spine curvature. Fig. 1 shows a timeline illustrating the different steps. Both metallic and polymeric spinal rods exist, with diameters ranging from 3.5 to 6.5 mm (Fig. 1a). During surgical intervention, rods are bent by the surgeon to reproduce the patient’s sagittal curvature (Fig. 1b). Bending is performed using specific tools such as the French Benders (FB), which often leaves permanent markings at the rod surface. Then, implants are attached directly to the spine with distal and proximal anchor points. The anchoring illustrated in Fig. 1c consists of three hooks placed proximally and two monoaxial pedicle screws placed distally (H3S2 construct) [4]. Some extra length is left available below the screws to anticipate patient growth. The rods are distracted at regular time intervals in order to avoid hindering the spine lengthening. Between each surgery, patient movements induce complex and varying stress states in the rods (Fig. 1d). A common very detrimental complication is the fracture of the rod (Fig. 1e). Such fracture events have been the subject of many studies, trying to elucidate the underlying mechanisms and to find ways to avoid the very invasive replacement surgery.

Several origins of rod failure have been suggested in the context of studies performed during the last decade. In 2011, Yang et al. analyzed records from 327 patients, with single and dual rod constructs, to identify failure risk factors [5]. It was found that (i) 15% of the patients experienced at least one fracture event; (ii) the thoracolumbar junction was identified as a frequent fracture site; (iii) looking at material impact, stainless steel rods exhibited higher fracture rates compared to titanium alloy. Yamanaka et al. identified from the fracture surface of Ti-6Al-4V alloy rods a fatigue failure mechanism [6]. In another study of broken rods of Hill et al., it was concluded that failure often occurs at locations where the rods had been highly bent [7]. In a more recent study, Ribesse et al. reached the same conclusion for pure titanium and cobalt chromium alloys [8]. Based on a beam bending model, thoracolumbar regions were also found to be the high risk fracture sites.

Four key factors can potentially affect the material lifetime:

(i) *The magnitude of the residual stresses resulting from manufacturing and shot peening.* Shot-peening is usually performed in order to induce a compressive stress state at the surface, a well-known way to delay fatigue crack initiation [9].

(ii) *The evolution of the residual stresses resulting from shaping.* During rod contouring, the surgeon bends the rod plastically. This changes the stress state locally, reorganizing the residual stress distribution and changing the accumulated plastic strain field.

(iii) *The generation of surface defects such as indentations.* During the shaping process, the bending tools often leave residual imprints at the surface of the rods. These imprints create stress concentrations, plastic strains and also change the local residual stress state.

(iv) *The accumulation of load cycles*. During operation in the body, rods are bent repeatedly due to patient movements. These fluctuating loads may induce the nucleation and propagation of fatigue cracks.

Taking into account all these factors within a predictive model is a scientific challenge. This study focuses primarily on the evolution of the residual stresses related to steps (i) and (ii).

Berti et al. investigated point (ii) using numerical methods [10]. The authors analyzed the radial distribution of the mean residual stress due to static contouring of the spine rod for two bending methods. Both techniques, FB and uniform contouring, resulted in the same stress profile. This profile, being the result of static contouring only, indicated the generation of tensile stresses on the concave side of the rod. The aim of our study is to further investigate the following questions about point (ii):

- Is it possible to develop a predictive model that captures the experimental trends about the residual stress profile and its evolution?
- How do hardening properties change the stress profile after bending?
- Does the bending angle imposed during contouring affect residual stresses?

- What is learned from such analysis in terms of guidelines for surgeons towards extending the lifetime of growing rods?

The objective is to provide answers to these questions using the following methodology. Internal stress measurements are first performed on unused rods and bent rods using the advanced focused ion beam milling technique combined with digital image correlation (FIB-DIC). The second step is to develop a numerical model that predicts the stress profile while accounting for shot peening and bending, and relying on mechanical tests to extract the hardening law. This requires a relatively advanced plasticity model, including kinematic hardening. After identification and validation, the model is used to perform a parameter study in order to elucidate the primary factors affecting the stress state.

2. MATERIALS AND METHODS

2.1 Materials

Ti-6Al-4V rods with 5.5 mm diameter were purchased from Medtronic Sofamor Danek under the tradename CD Horizon® Legacy™ System. The tensile properties as well as local hardness variations along a radius of the rod were determined by mechanical testing. In addition, 10 cm length specimens were extracted to perform residual stress measurements in straight and bent rods.

The tensile test samples were machined into cylindrical dog-bone shape with a diameter of 4 mm representative of the core of the rod (see Fig. 2a). The tests were carried out until fracture on a Zwick Roell stress rig. The applied displacement rate was set to 1 mm/min.

Fig. 2b shows the uniaxial tension response in terms of the variation of the true stress

$$\sigma = \frac{F}{A_0}\left(1 + \frac{u}{L_0}\right), \tag{1}$$

as a function of the true strain

$$\epsilon = \ln\left(\frac{L}{L_0}\right). \tag{2}$$

where *F* is the tensile force, A_0 is the initial cross-section area, *u* is the elongation and L_0 and *L* are respectively the initial and the deformed gage length. Three tests were performed to control reproducibility.

The following properties were determined from the uniaxial tension response, shown in black in Fig. 2b: Young's modulus *E*=113 ± 1 GPa; yield stress $\sigma_{0.2\%}$=1000 ± 5 MPa.

Finally, nanoindentation tests were performed with an Agilent Technologies NanoIndenter G200 using a Berkovich tip of known stiffness. Sixteen indents were performed both on the transverse cross section of the rod at the center as well as close to the surface. The hardness is equal to 4.1 ± 0.2 GPa at the surface and 3.8 ± 0.1 GPa in the core along the axis of the rod. The surface hardness is thus larger by about 10% compared to the center, which is attributed to the accumulation of plastic deformation due to shot peening.

2.2 Methods

2.2.1 Rod bending

Two 10-cm-long samples were cut out of the as-received Ti-6Al-4V rod, and subsequently bent using the French Bender device by a trained surgeon. The goal was to apply the surgical practice as closely as possible. Two bending amplitudes were considered and the corresponding contouring angles were measured after elastic springback, using a profile projector (Mitutoyo PJ 300, Illinois, USA). The latter angle was measured between the two tangents aligning with the two ends of the rod. The two specimens had residual bending angle equal to 4° and 13°, respectively.

2.2.2 FIB-DIC ring-core milling

Among all techniques devoted to residual stress measurement, the FIB-DIC method provides a high spatial resolution and the possibility of measuring very close to the surface of the material.

Both samples were cut longitudinally (see Fig. 3a) and the cross-sections were electrochemically polished during 10 min using a current density of 2 kA/m^2 in an electrolyte containing 700 ml/l ethanol, 300 ml/l isopropanol, 60 g/l $AlCl_3$ and 250 g/l $ZnCl_2$. This ensured removal of the layer exposed to cutting and grinding residual stresses [11]. The residual stress along the longitudinal (x) and radial (y) directions was evaluated at ten evenly spaced locations over the cross-section of each sample by means of focused ion beam (FIB) ring-core milling and digital image correlation [12]. This technique consisted of several steps. First, a pattern suitable for digital image correlation (DIC) was created by depositing a thin Pt layer via sputtering and then performing two FIB scanning passes on the area of interest. Next, a micropillar (diameter 5 µm) was machined incrementally by FIB milling in 40 steps of 125 nm (see Fig. 3b). After each milling step, ten images of the top surface of the pillar were taken by scanning electron microscopy (SEM) with a pixel size of 8 nm and an electron beam energy of 5 keV. The micropillar undergoes a gradual strain relief upon progressive milling, which was measured via DIC on the SEM images. For the DIC analysis, a grid with a marker spacing of 12 pixels was used and the marker displacements were averaged over ten images for each milling step. The DIC analyses were carried out using an open source software *Digital Image Correlation and Tracking* available on MathWorks [13]. This produced a relief strain curve, in the x and y directions, as a function of milling depth. These curves were fitted to the master curve function as described by Korsunsky et al. [14] to obtain the total relief strain in the x ($\Delta\varepsilon_x$) and y ($\Delta\varepsilon_y$) directions. Complete stress relief was achieved when the total milling depth was equal to the pillar diameter [14]. Most pillars include more than one grain which justifies the approximation of using isotropic elasticity [15]. Combined with the assumption of non-equi-biaxial stress state, the residual stress in the x direction (σ_{xx}) and in the y direction (σ_{yy}) were determined using Hooke's law as:

$$\sigma_{xx} = -\frac{E}{(1-\nu^2)}\left[\Delta\varepsilon_x + \nu\Delta\varepsilon_y\right], \tag{3}$$

$$\sigma_{yy} = -\frac{E}{(1-\nu^2)}\left[\nu\Delta\varepsilon_x + \Delta\varepsilon_y\right]. \tag{4}$$

with E and Poisson ratio ν equal to 113 GPa and 0.3, respectively. The error bars, which represent a 95% confidence interval, were calculated as described by Lunt et al. [16]. This includes the error due to DIC tracking, the error caused by fitting the data to the master relief curve, and the error caused by the assumption of isotropy.

3. EXPERIMENTAL RESULTS

Fig. 3c shows the variation of stress in direction *x* along the rod axis as a function of position as deduced from the FIB-DIC method. The surface layers of the as-received (straight) rod are under 800 MPa compression[2] over a thickness of 0.3 mm from the surface. Such stress state may be expected after shot peening.

After 4° and 13° bending, Fig. 3c shows that the residual stress profile inside the Ti-6Al-4V bent rods becomes more complex. At the surface of the concave part of the rod (i.e. y=-2.75 mm), the stress is slightly compressive reaching -150 MPa. Within the next two millimeters, the stress first increases slightly to reach a few hundreds of MPa in tension, before returning to a compressive stress of about -500 MPa. Close to the core, a steep inversion of the stress state is observed, resulting in a tensile state on the other side of the core, decreasing gradually to reach a compressive state again towards the convex surface (i.e. y=2.75 mm) of about -500 MPa. Both surfaces remain thus in compression but the magnitude of the residual stress is reduced especially on the concave part. Note that the residual stress profile does not vary very much between 4° and 13° bending, especially near the concave surface.

[2] In vivo broken rods show crack propagation along the *y* direction. In this study, even if there is no crack in the model, we will focus on the stress component σ_{xx}, which will be the driving force for fatigue crack propagation.

4. MODELLING AND SIMULATION

The model must account for the impact of both shot peening and bending to predict the residual stress profile. The mechanical history of the material at the periphery of a growing rod is complex. Initially, the rod surface is uniformly compressed during the shot peening stage. Then, when the surgeon bends the rod with a FB, the axial segments along the convex side are stretched, while the axial segments on the concave side experience further compression. During the elastic unloading after bending, the axial segments extend on the concave side, while contraction occurs on the opposite side.

4.1 Description of the models

To select the most representative constitutive plasticity model, both isotropic hardening and kinematic hardening models have been compared.

a. Isotropic hardening model

As illustrated in Fig. 4a, during a uniaxial solicitation, the center of the elastic domain of a plastically loaded isotropic material does not move but the size of the domain increases resulting in the same yield stress in tension and in compression. The isotropic hardening model of his study assumed a constant hardening slope $d\sigma_Y/dp$ where σ_Y is the current yield stress and *p* the accumulated plastic strain.

b. Kinematic hardening model

The mechanical response during a uniaxial solicitation for purely kinematic hardening is illustrated in Fig 4b. During the loading, the elastic domain maintains a constant size equal to 2 σ_0 with σ_0 the yield stress, but its center progressively shifts due to heterogeneous residual stress developing at microscale (also called "backstress") and which have a different origin related to the microstructure compared to macroscopic residual stress profile on which this study focuses.

Under multiaxial loading condition, the backstress is a tensor $\boldsymbol{X}$ and one possible law describing its evolution has been proposed by Chaboche and Marquis [17] in the form:

$$\dot{\boldsymbol{X}} = A\dot{\boldsymbol{\epsilon^p}} - B\boldsymbol{X}\dot{p}, \tag{5}$$

where *A* and *B* are two scalar parameters. Their ratio *A/B* defines the maximum amplitude of the backstress, whereas $\dot{\boldsymbol{\epsilon^p}}$ is the plastic strain rate and $\dot{p}$ is the rate of increase of the accumulated plastic strain. In the following, the amplitude of deformation will be essentially quantified by the bending angle, which is the operating parameter. In the practice, the surgeon does indeed not control the amplitude of $\boldsymbol{\epsilon^p}$.

4.2 Finite element model

The elastoplastic linear isotropic hardening model is directly available in the commercial Finite Element (FE) solver Abaqus while the elastoplastic non-linear kinematic hardening model from Chaboche and Marquis was implemented through a user-defined material law UMAT of Abaqus based on implicit Newton–Raphson method [18]. The bending is symmetrical with respect to two planes. Firstly, the two outer rollers move in an mirror-image motion, creating an initial symmetry perpendicular to the central tool. Then, once the bar has been bent, a plane parallel to the bending plane and located at mid-thickness in the bar constitutes the second plane of symmetry. Taking advantage of those symmetries, only ¼ of the rod was modelled in 3D (see Fig. 5a). In order to avoid numerical locking due to the nearly-incompressible response, C3D8R three-dimensional linear solid elements were adopted to simulate the bending process. The diameter of the rod was discretized into 22 elements while 33 elements were used along the length.

At first, the model aimed at replicating the state of the rod prior to bending. Shot peening introduces a compressive stress field in the near surface region. Effectively simulating the shot impacts in a realistic direct way requires advanced numerical models out of the scope of the present study. Here, in order to capture the effect of shot peening, a different material law was assigned to the outer layer to accommodate the local variation of the yield strength (see section 4.3.a) and the residual stresses were considered through a fictitious thermal step forcing a dilation inside a layer of thickness *h* of one element at the surface (0.22mm). This induces compressive hoop and axial stress equal to -820 MPa. As the equivalent von Mises stress reaches the yield point, plastic deformation is induced and the external elements develop a backstress change during this step.

Subsequently, the bending was simulated by describing the kinematics imposed by the French Bender. Fig. 5b shows the geometry of the rod and of the tool assembly after applying the two mirror symmetries to represent the complete structure. The tool is composed of two pins, a fixed one, located at the central symmetry plane, and a mobile one. The position of the center of the mobile pin was set and maintained 35 mm away from the center of the fixed pin. The motion of the mobile pin is a circumferential rotation applied around an axis passing through the center of the fixed pin. All dimensions were extracted from a real FB. After checking that the deformability of the tool (slight flattening of the contact surface) did not affect the results significantly, the tools were modeled as rigid bodies. The friction coefficient was set to 0.2. The angular motion of the mobile pin led to the right configuration after unloading (i.e. after elastic springback).

4.3 Results

a. *Identification and validation of the models*

The rod was partitioned into two parts, the core and the skin, to capture the local effect of shot peening, each one obeying a different hardening law. Both kinematic and isotropic hardening models were identified. The core response was imposed in order to match the uniaxial stress strain response obtained experimentally on a dog bone specimen as illustrated in Fig. 6a. In the shot peened region, the material is known to exhibit an heterogeneous stress field [19]. The combination of tensile and compressive stresses in this area leads to select a lower elastic limit for the macroscopic mechanical response, while the *A* and *B* parameters were adjusted to retrieve a similar tensile strength after 8% deformation as illustrated in Fig. 6b. The identified values are gathered in Table 1 with parameters selected for the isotropic model.

The residual stresses predicted with both isotropic or kinematic hardening have been compared to the stress distributions determined by FIB-DIC. As illustrated in Fig. 7, for identical $\sigma_{xx}^{initial}$ profiles (Fig. 7a), isotropic and kinematic hardening result in two distinct σ_{xx}^{final} profiles (Fig. 7b). The FEA stress contours for the kinematic hardening model are represented below each plot. At the concave side of the bent rod (y=-2.75 cm), the compressive stresses measured experimentally are not captured by isotropic hardening, validating the choice of kinematic hardening. Note that we played with a large range of isotropic hardening and could never capture the experimental trends with reasonable parameters.

b. Parametric study

After identification and validation of the model, a parametric study was performed to determine the evolution of the residual stresses at the likely site of cracking initiation. The thoracolumbar junction was identified as the most at-risk location [5,6,8,20]. Moreover, fractography analysis indicates that cracks systematically initiate on the dorsal side of the rod and propagate towards the ventral side [7,8]. At this location, the rod is usually bent in a lordotic configuration [21], inducing the most likely site of fatigue crack initiation at the concave side of the rod (i.e. at y=-2.75mm in our model).

The residual stress state at the rod surface is essentially controlled by seven parameters :

$$\sigma_{xx}^{final} = F(E,\ \sigma_0^{skin},\ A^{skin},\ B^{skin},\ \sigma_{xx}^{initial},\ h,\ R), \tag{6}$$

where E is the Young's modulus ; σ_0^{skin}, A^{skin} and B^{skin} are hardening parameters; $\sigma_{11}^{initial}$ is the initial stress state imposed to the surface elements after the shot-peening step 1 through the fictitious thermal loading, h is the thickness of the surface shell which undergoes compressive stresses and R is the radius of the rod. Equation (6) is non-dimensionalized as follows

$$\frac{\sigma_{xx}^{final}}{E} = F\left(\frac{\sigma_0^{skin}}{E}, \frac{A^{skin}}{E},\ B^{skin}, \frac{\sigma_{xx}^{initial}}{E},\ \frac{h}{R}\right). \tag{7}$$

The master set of parameters, presented in Table 2, was defined as the one providing the best match with experiments as a result of the identification. The parameters associated to the core elements were fixed and all the other parameters can be varied to assess their impact. For the sake of simplicity, the parameters $\sigma_0^{skin}, A^{skin}$, B^{skin}, are noted as σ_0, A, B in the sequel.

In order to analyze the impact of the surgeon's practice, Figure 8 depicts the effect of the bending angle on the final stress level by plotting the variation of the final near surface residual stress state as a function of the bending angle for three initial stress levels produced by shot-peening. For this set of simulations, the angular motion of the mobile pin was tuned to produce pre-selected contouring angles after springback. The σ_{xx}^{final}/E ratio increases steeply at very low angles, levels off, reaches a maximum and then decreases slightly at larger angles.

The angular motion of the mobile pin was fixed to 0.62 rad for all the following simulations. All imposed bending angles after springback lie between 9°5' and 12°3'. As the bending angle was found to have a limited effect, we did not attempt to reach exactly the same final angle for each set of material parameters.

Figure 9 shows the variation of σ_{xx}^{final}/E with (a) A/E, (b) *B*, (c) σ_0/E and (d) h/R for three different initial stress levels. Increasing A/E reduces the magnitude of σ_{xx}^{final}/E see Fig. 9a. For high ratio of A/E, a compressive residual stress is produced at the concave rod surface. When the parameter *B* increases, σ_{xx}^{final}/E gradually rises as shown in Fig. 9b. This effect is less important than the impact of the A/E value.

Increasing σ_0/E leads to a general increase of σ_{xx}^{final}/E as shown in Fig. 9c. Again, a compressive residual stress state is generated at the concave rod surface for low σ_0/E ratio. The effect of the thickness of the compressive layer on the variation of σ_{xx}^{final}/E with respect to the rod diameter in Fig. 9d shows that the final stress state is independent of h/R for the three shot peening intensities.

Regarding the effect of $\sigma_{xx}^{initial}/E$ adressed in both Fig. 8 and Fig. 9, the generation of a compressive initial stress state leads to a decrease σ_{xx}^{final}/E. If the initial stress state is sufficiently low, bending leads to a compressive residual stress state at the surface. The relationship between $\sigma_{xx}^{initial}/E$ and σ_{xx}^{final}/E is not perfectly linear.

5. DISCUSSION

Residual stresses play a major role in mitigating fatigue crack initiation and growth, which is the mechanism identified as leading to the failure of the growing rods [6–8]. Currently few studies investigated the residual stresses in growing rods, prior and during their implantation. Analyzing and understanding the residual stress distribution and their dependence on the materials, geometrical and loading parameters is key to guide towards enhancing rod durability through surgeon techniques and/or better material selection. Comparing numerical simulations results with measured stress fields improves the accuracy of the analyses and provides a better starting point to observe the impact of various parameters.

5.1 Prediction of the residual stress profile

The first aim of this study was to create a numerical model capturing the residual stress field measured by FIB-DIC after FB bending, while accounting for the initial stress field induced by shot peening. Fig. 7b illustrated that an isotropic model, such as the one used in the study of Berti et al. [10], is not able to correctly predict the compressive stresses found experimentally at the concave rod surface. A core element of novelty of our approach was thus to combine the initial stress field with a kinematic hardening-based model. As illustrated in the study of Zhang, the material model selection is key when performing residual stress distribution analysis [22]. Compared to isotropic hardening, for which the yield surface expands with plastic deformation, the surface undergoes a shift if the hardening is a kinematic nature. Fig. 10 illustrates three scenarios: (i) a growth rod made of a material with isotropic hardening undergoing the following loading sequence: shot peening, forward bending and bending unloading; (ii) a growing rod made of a material with kinematic hardening (loading sequence without shot peening); (iii) a growing rod made of a material with kinematic hardening and full loading sequence. The model shows that a springback may involve reverse plastic deformation with kinematic hardening while it is not the case for isotropic hardening. By combining a kinematic model with the shot peening process, the flow surface shifts twice towards the compression zone during the first two plasticity events, shot peening and forward bending. This shift mitigates the tendency of ending up with a tensile state near the surface after springback. The model eventually captures the compressive residual stress at the concave surface of the rod compared to the literature.

5.2 Towards favoring compressive residual stresses

The second aim of this study was to identify the main parameters that could enhance the fatigue life from the perspective of the residual stress state. As explained in Section 4.3.b, shifting the residual stresses towards the compressive regime at the concave surface of the rod could help increasing the fatigue lifetime of the rod.

Various ways to reduce the amplitude of residual stresses have been suggested in the literature relative to the distraction frequency, contouring technique and loading configuration. In multiple studies, Agarwal et al. analyzed the optimal distraction frequency [23,24]. When the time period between two distractions is reduced, the stresses in the rods decrease. In the study of Berti et al. [10], the authors compared the mean residual stress radial evolution due to static contouring for two bending methods by the mean of numerical simulations. Both techniques, FB and uniform contouring, resulted in an identical stress profile, introducing tensile stresses at the concave side of the rod. Based on these results, Piovesan et al. assessed the fatigue behavior for bent rods loaded in lordotic and kyphotic configurations. By moving, patients add a dynamic stress state in the rod. If the rod is placed in a lordotic configuration, the sum of the two contributions to the stress amplitude will increase the risk of fatigue failure compared to a kyphotic configuration [21]. Finally, using their numerical method to describe the local residual stress distribution induced by contouring, Berti et al. introduced a sensitivity analysis by changing hardening modulus in the material law. Controlling the final radius of curvature, ideal elastoplastic material showed the highest levels of residual stresses [10].

Here, we performed a parametric analysis after proper non-dimensional reduction. The intent was to provide trends about the most relevant parameters that could be potentially manipulated to reduce the local residual stress level, but not necessarily to quantify the very precise stress level in the rod. First, the bending angle applied by the surgeon with a FB is examined to question their practices in Section 5.2.1. After that, processing parameters are addressed such as the shot peening depth and intensity to determine the impact of shot peening on the residual stress evolution in growing rods in Section 5.2.2. Finally, we analyze material properties, such as yield strength and hardening coefficients to give guidelines about material selection, in Section 5.2.3.

5.2.1 Guiding better surgeon practice

The plastic deformation associated to the rod bending imposed to conform to the spine morphology fully removes the initial compressive stresses at the rod surface and this even for low bending angle. The model (and the experiments) show that applying a small or a large angle does not result in large variations of σ_{xx}^{final}/E. A slight decrease of σ_{xx}^{final}/E is even found for the largest angles suggesting that the bending angle is not responsible for a decrease of the fatigue properties from a residual stress viewpoint. This trend may not be true for all sets of parameters and we cannot thus conclude that surgeons can apply any bending angle without any impact on fatigue lifetime of the rod. The main reason for the limited effect is the small amount of plastic deformation induced by bending, negligible compared to the total plastic deformation accumulated during shot peening and later during life due to patient movements.

5.2.2 Processing parameters

Considering the processing parameters, the initial compressive stress upon shot peening has a positive impact on the final surface stress level. The analysis of the effect of $\sigma_{xx}^{initial}/E$ demonstrates the efficiency of shot peening even at locations that undergo subsequent plastic deformation. In addition to an initial compressive stress state, this process goes along with an initial yield surface shift due to local plastic deformation. It should be noticed that the initial magnitude of the compressive stress does not reveal the final compressive stress level after bending and springback. Depending on the parameter set, a certain amount of compressive stress should be introduced during shot peening in order to produce surface compressive stress after bending. The depth of the outer compression ring plays a negligible role on the intensity of the final stress level at the surface. The main advantage of increasing h/R is to reduce the stress level in the inner part of the rod. This could reduce the propagation rate of a potential fatigue crack.

5.2.3 Material selection

The stress level σ_{xx}^{final}/E significantly depends on σ_0/E , A/E and *B*. Material selection for biomedical implant aims at selecting materials with stiffness close to the one of bone. The flexibility is thus higher on parameters σ_0 and *A* than on *E*. Lowering the yield strength and keeping the same Young's modulus will decrease the stress level in the rod. The main reason for this effect is explained by the unloading of the rod after bending. By reducing σ_0, reverse plasticity is more easily produced.

Considering hardening properties, Fig. 7b demonstrates that material exhibiting kinematic hardening develop a specific residual stress profile, with reduced residual stresses at the concave side of the rod. In their study, Berti et al. concluded that the (isotropic) hardening of elastoplastic materials reduces the amplitude of tensile residual stresses [10]. Our results indicate that kinematic hardening can improve residual stresses even more. According to Fig. 9a and Fig. 9b, the saturating value of the backstress (*A/B* ratio) should be large, and it should not be reached too quickly during bending process (thanks to a small *B* value). Such kinematic hardening induces a stress gradient in the bent rod and this promotes compressive residual stresses after unloading. This tends to be consistent with the conclusions of Berti et al [10].

From this sensitivity analysis, some recommendations for microstructural improvements can be formulated. Indeed, the yield stress and back stress are related to the grain size following respectively:

$$\sigma_0 = \sigma_p + k/\sqrt{d}, \tag{8}$$

$$\sigma_b = \frac{M\mu bn}{d}, \tag{9}$$

with σ_p the frictional stress resisting the motion of the gliding dislocation (so called Peierls stress), *k* the Hall-Petch constant, *d* the grain size, σ_b the backstress, *M* the Taylor factor, *μ* the shear modulus, *b* the magnitude of the Burger's vector and *n* the mean number of the dislocations in a pile-up.

These equations, combined with the results of the parametric analyses, suggest that the grain size has an antagonistic effect on the magnitude of the final residual stress. Indeed, equation (8) indicates that an increase in grain size reduces the yield strength, which in turn reduces the residual stress in the growing rods. Conversely, equation (9) shows that by increasing the grain size, the material will exhibit less backstress and therefore less kinematic hardening, which will increase the value of residual stress in growth rods. Based on these relationships, one could potentially determine an ideal grain size for each shot peening intensity, an idea left for further investigations.

5.3 Limitations of the model and perspectives

As an additional possible contribution to the mechanical behavior, texture and mechanical anisotropy were not taken into account in our analysis. In their study, Everaerts et al. estimated the variation of the residual stress, for a Ti-6Al-4V bent bar, to be equal to 150 MPa depending on the orientations of the grains due to Young's modulus and Schmid factor fluctuations [15]. Another source of known anisotropy in titanium alloys is the α phase which presents for instance an asymmetry for <c+a> slip between tension and compression [25]. These aspects were disregarded. Moreover, the possible development of a deformation texture during shaping process was not addressed but could be taken into account in the numerical model to produce more realistic results. The analysis considered only kinematic hardening, but some degree of isotropic hardening should also be ideally introduced which would modify at least quantitatively the prediction. We, however, think that the main shortcoming of our work is more the absence of anisotropy than of some minor isotropic strain hardening effect also in view of the low strain hardening capacity of Ti-6Al-4V. Understanding these effects may help further refining the material selection for growing rods.

Regarding the model geometry, the tool used to simulate the bending process is based on the geometry of FB. Surgeons could potentially use other bending techniques, such as so called "in situ benders". In the literature, the analysis of the residual stresses resulting from various bending technique has already been performed assuming isotropic hardening [10,26]. Nevertheless, the result of the parameter study in Section 4 tend to show that no first order effect is expected. But, maybe, the marking due to the contact with the bend tool could vary from one device to another and lead to specific local deleterious residual stress concentration not investigated here.

Finally, residual stresses are not the only points of concern regarding the fatigue life of a system. In the literature, the impact of prestraining on the fatigue behavior has already been studied. Chiou & Yang 2012 found that prestraining is detrimental to fatigue lifetime for similar stress amplitude tests [27]. However, in the studies of Kang & al 2007 and Froustey & Lataillade 2008, the residual fatigue lifetime was not impacted in the same way based on the alloy considered [28,29]. Therefore, the coupling of these numerical analyses with experimental fatigue tests on bent rods seems very promising to determine the impact of bending on fatigue life while having a deeper understanding of the residual stresses present in the rods before fatigue loading. The later contribution for growing rod is currently under investigation by running complex fatigue tests on bent rods.

6. CONCLUSION

This paper proposed a new model for predicting the residual stresses in growing rods, identified and validated based on original experimental results generated with the FIB-DIC micro-ring method. On the basis of this model, parametric analyses have been carried out to identify the parameters that could play a major role in the objective of mitigating the residual stress level and, ideally, create compressive stresses. The main findings of the study are the following:

- Proper account of the kinematic hardening nature of the plastic behavior is essential to predict the local evolution of the residual stress profile in particular to capture the correct magnitude of the compressive stresses on both concave and convex sides of the rod after bending.
- The surgeon practice in terms of bending manipulation does not play a significant role on setting the final magnitude of the near surface residual stresses where fatigue initiates, but shot peening does.
- In the context of the present findings, the best material choice is with low initial yield stress and higher kinematic hardening. Guidelines on microstructural modifications involve contradictory requirements. Materials with smaller grain size, higher mobile dislocation density and larger second phase particle, will exhibit more kinematic hardening but with a higher yield strength.

An attractive option for future research is to investigate multiphase alloys with large strength mismatch among the phase with one relatively soft phase, which will potentially combine low to moderate initial yield strength and significant kinematic hardening.

ACKNOWLEDGMENT

The authors wish to thank Colin Laville of Université catholique de Louvain for his technical assistance in section 4.2. Computational resources have been provided by the supercomputing facilities of the Université catholique de Louvain (CISM/UCL) and the

Consortium des Équipements de Calcul Intensif en Fédération Wallonie Bruxelles (CÉCI) funded by the Fond de la Recherche Scientifique de Belgique (F.R.S.-FNRS) under convention 2.5020.11 and by the Walloon Region. LD is mandated by the FSR-FNRS.

REFERENCES

[1] Cunin, V., 2015, “Early-Onset Scoliosis-Current Treatment,” Orthop. Traumatol. Surg. Res., **101**(1), pp. S109–S118.

[2] Fletcher, N. D., and Bruce, R. W., 2012, “Early Onset Scoliosis: Current Concepts and Controversies,” Curr. Rev. Musculoskelet. Med., **5**(2), pp. 102–110.

[3] Yazici, M., and Olgun, Z. D., 2013, “Growing Rod Concepts: State of the Art,” Eur. Spine J., **22**(SUPPL.2).

[4] Miladi, L., and Mousny, M., 2014, “A Novel Technique for Treatment of Progressive Scoliosis in Young Children Using a 3-Hook and 2-Screw Construct (H3S2) on a Single Sub-Muscular Growing Rod: Surgical Technique,” Eur. Spine J., **23**(SUPPL. 4).

[5] Yang, J. S., Sponseller, P. D., Thompson, G. H., Akbarnia, B. A., Emans, J. B., Yazici, M., Skaggs, D. L., Shah, S. A., Salari, P., and Poe-Kochert, C., 2011, “Growing Rod Fractures: Risk Factors and Opportunities for Prevention,” Spine (Phila. Pa. 1976)., **36**(20), pp. 1639–1644.

[6] Yamanaka, K., Mori, M., Yamazaki, K., Kumagai, R., Doita, M., and Chiba, A., 2015, “Analysis of the Fracture Mechanism of Ti-6Al-4V Alloy Rods That Failed Clinically after Spinal Instrumentation Surgery,” Spine (Phila. Pa. 1976)., **40**(13), pp. E767–E773.

[7] Hill, G., Nagaraja, S., Akbarnia, B. A., Pawelek, J., Sponseller, P., Sturm, P., Emans, J., Bonangelino, P., Cockrum, J., Kane, W., and Dreher, M., 2017, “Retrieval and Clinical Analysis of Distraction-Based Dual Growing Rod Constructs for Early-Onset Scoliosis,” Spine J., **17**(10), pp. 1506–1518.

[8] Ribesse, A., Ismail, K., Croonenborghs, M., Irda, N., Miladi, L., Jacques, P. J., Mousny, M., and Pardoen, T., 2021, “Fracture Mechanisms in Ti and Co–Cr Growing Rods and Impact on Clinical Practice,” J. Mech. Behav. Biomed. Mater., **121**(May).

[9] Suresh, S., 1998, *Fatigue of Materials*, Cambridge university press.

[10] Berti, F., La Barbera, L., Piovesan, A., Allegretti, D., Ottardi, C., Villa, T., and Pennati, G., 2018, “Residual Stresses in Titanium Spinal Rods: Effects of Two Contouring Methods and Material Plastic Properties,” J. Biomech. Eng., **140**(11), pp. 111001-1-111001–8.

[11] Everaerts, J., Salvati, E., and Korsunsky, A. M., 2019, “Nanoscale Depth Profiling of Residual Stresses Due to Fine Surface Finishing,” Adv. Mater. Interfaces, **6**(21), pp. 1–5.

[12] Korsunsky, A. M., Sebastiani, M., and Bemporad, E., 2009, “Focused Ion Beam Ring Drilling for Residual Stress Evaluation,” Mater. Lett., **63**(22), pp. 1961–1963.

[13] Melanie Senn, 2016, “Digital Image Correlation and Tracking,” MATLAB Cent. File Exch., p. 1 [Online]. Available: https://www.mathworks.com/matlabcentral/fileexchange/50994-digital-image-correlation-and-tracking.

[14] Korsunsky, A. M., Sebastiani, M., and Bemporad, E., 2010, “Residual Stress Evaluation at the Micrometer Scale: Analysis of Thin Coatings by FIB Milling and Digital Image Correlation,” Surf. Coatings Technol., **205**(7), pp. 2393–2403.

[15] Everaerts, J., Salvati, E., Uzun, F., Romano Brandt, L., Zhang, H., and Korsunsky, A. M., 2018, “Separating Macro- (Type I) and Micro- (Type II+III) Residual Stresses by Ring-Core FIB-DIC Milling and Eigenstrain Modelling of a Plastically Bent Titanium Alloy Bar,” Acta Mater., **156**, pp. 43–51.

[16] Lunt, A. J. G., and Korsunsky, A. M., 2015, “A Review of Micro-Scale Focused Ion Beam Milling and Digital Image Correlation Analysis for Residual Stress Evaluation and Error Estimation,” Surf. Coatings Technol., **283**, pp. 373–388.

[17] Doghri, I., 2000, *Mechanics of Deformable Solids: Linear, Nonlinear, Analytical and Computational Aspects.*, Springer Science & Business Media.

[18] Zinovev, A., Delannay, L., and Terentyev, D., 2021, “Modeling Strain Hardening during Cyclic Thermal Shock Tests of Tungsten,” J. Nucl. Mater., **546**, p. 152776.

[19] Breumier, S., 2021, “Methodology for Shot-Peening Induced Intragranular Residual Stress Prediction,” Université de Lyon; Ecole Polytechnique de Montréal.

[20] Smith, J. S., Shaffrey, C. I., Ames, C. P., Demakakos, J., Fu, K. M. G., Keshavarzi, S., Carol, C. M., Deviren, V., Schwab, F. J., Lafage, V., and Bess, S., 2012, “Assessment of Symptomatic Rod Fracture after Posterior Instrumented Fusion for Adult Spinal Deformity,” Neurosurgery, **71**(4), pp. 862–867.

[21] Piovesan, A., Berti, F., Villa, T., Pennati, G., and La Barbera, L., 2019, “Computational and Experimental Fatigue Analysis of Contoured Spinal Rods,” J.

Biomech. Eng., **141**(4), p. 044505.

[22] Zhang, Z. T., and Hu, S. J., 1998, “Stress and Residual Stress Distributions in Plane Strain Bending,” Int. J. Mech. Sci., **40**(6), pp. 533–543.

[23] Agarwal, A., Agarwal, A. K., Jayaswal, A., and Goel, V. K., 2017, “Outcomes of Optimal Distraction Forces and Frequencies in Growth Rod Surgery for Different Types of Scoliotic Curves: An In Silico and In Vitro Study,” Spine Deform., **5**(1), pp. 18–26.

[24] Agarwal, A., Goswami, A., Vijayaraghavan, G. P., Srivastava, A., Kandwal, P., Nagaraja, U. B., Goel, V. K., Agarwal, A. K., and Jayaswal, A., 2019, “Quantitative Characteristics of Consecutive Lengthening Episodes in Early-Onset Scoliosis (EOS) Patients with Dual Growth Rods,” Spine (Phila. Pa. 1976)., **44**(6), pp. 397–403.

[25] Roberts, W., Gong, J., Wilkinson, A. J., and Tarleton, E., 2020, “Tension–Compression Asymmetry of 〈c+a〉 Slip in Ti–6Al,” Scr. Mater., **178**, pp. 119–123.

[26] Kim, K. D., Panchal, R., Moldavsky, M., Wang, W., and Bucklen, B. S., 2020, “Effects of Pre-Contoured and in Situ Contoured Rods on the Mechanical Strength and Durability of Posterior Cervical Instrumentation: A Finite-Element Analysis and Scanning Electron Microscopy Investigation,” Spine Deform., **8**(4), pp. 569–576.

[27] Chiou, Y. C., and Yang, J. K., 2012, “The Effects of Pre-Deformation on the Subsequent Fatigue Behaviors of SUS 430 Stainless Steel in Load-Control,” Int. J. Solids Struct., **49**(23–24), pp. 3263–3268.

[28] Kang, M., Aono, Y., and Noguchi, H., 2007, “Effect of Prestrain on and Prediction of Fatigue Limit in Carbon Steel,” Int. J. Fatigue, **29**(9–11), pp. 1855–1862.

[29] Froustey, C., and Lataillade, J. L., 2008, “Influence of Large Pre-Straining of Aluminium Alloys on Their Residual Fatigue Resistance,” Int. J. Fatigue, **30**(5), pp. 908–916.

Table Caption List

Table 1 Core and skin parameters for the kinematic hardening and isotropic hardening models for Ti-6Al-4V alloy

Table 2 Master set of parameters for Ti-6Al-4V alloy

Figure Captions List

Fig. 1 Spine correction by growing rod surgery: (a) initial straight rods with specific diameter; (b) contouring by the surgeon using a French Bender tool ; (c) anchoring to the spine (here H3S2 construct); (d) dynamic loads during daily life; (e) rod failure in some circumstances

Fig. 2 Uniaxial tensile tests: (a) samples geometry; (b) true stress – true strain uniaxial tension response from three Ti-6Al-4V specimens

Fig. 3 (a) Coordinate system for the bent rod indicating the location of the FIB-DIC measurements (b) SEM images of the milled area with DIC pattern, before and during milling steps (c) Radial profile of the residual stress along the rod axis in a Ti-6Al-4V (grey circle) unbent (unloaded) rod, (blue triangle) 4° bent rod, (red square) 13° bent rod measured by FIB-DIC.

Fig. 4 Graphical representation of a load cycle under uniaxial stress condition based on either (a) isotropic hardening, or (b) kinematic hardening – inspired from [17]

Fig. 5 (a) Illustration of FE mesh in the 1/4 rod using taking advantage of symmetries, (b) illustration of the complete structure (rod + tool) reconstructed using symmetries showing the configuration before and during contouring.

Fig. 6 Cyclic stress - strain curves for the identification of the isotropic hardening and kinematic hardening models (a) for the core of the rod compared to the tensile stress strain curve from experiment and, (b) for the skin of the rod

Fig. 7 Superposition of FIB-DIC measurements and simulations results obtained with either kinematic or isotropic models of radial profile of the longitudinal residual stress for (a) a straight rod, (b) a rod bent at 13 degrees, made of Ti-6Al-4V supported by the respective FEA stress contour predicted with the kinematic hardening model

Fig. 8 Variation of the stress along the rod axis at the concave rod surface after bending as a function of bending angle α

Fig. 9 Variation of near surface residual longitudinal stress at the concave rod surface normalized by Young’s modulus after bending as a function of A/E, B, σ_0/E and h/R. The reference set of parameters are A/E= 0.05, B=5, σ_0/E=0.005 and h/R= 0.08 with a bending angle ranging from 9°5’ and 12°3’.

Fig. 10 Schematic representation of yield surface during the bending process at concave surface of the rod for (a) isotropic hardening with shot peening, (b) kinematic hardening without shot peening and (c) kinematic hardening with shot peening. The final stress state is highlighted by a blue color when compressive and in red when in tension.

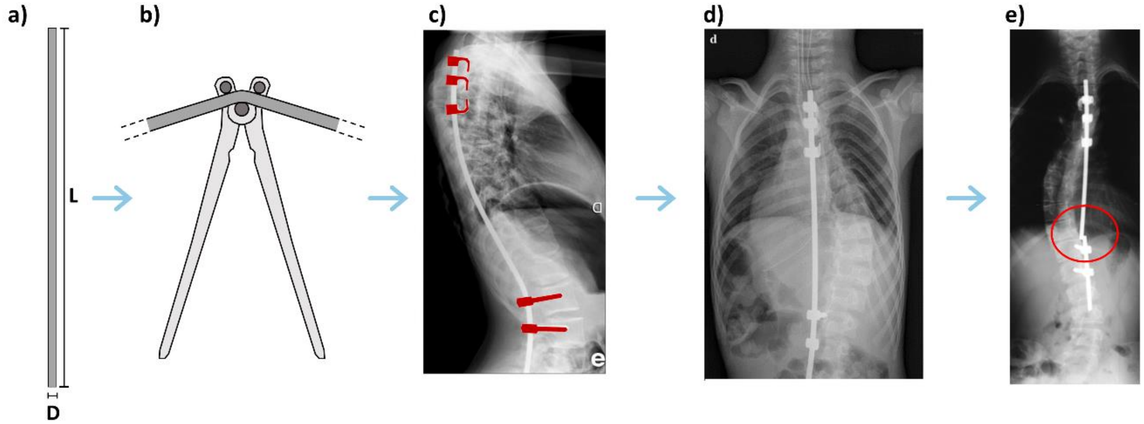

Figure 1

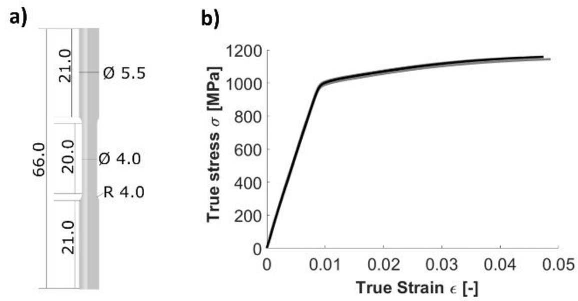
a)
21.0
Ø 5.5
66.0
20.0
Ø 4.0
R 4.0
21.0
b)
1200
1000
800
600
400
200
0
True stress σ [MPa]
0
0.01
0.02
0.03
0.04
0.05
True Strain ϵ [-]

Figure 2

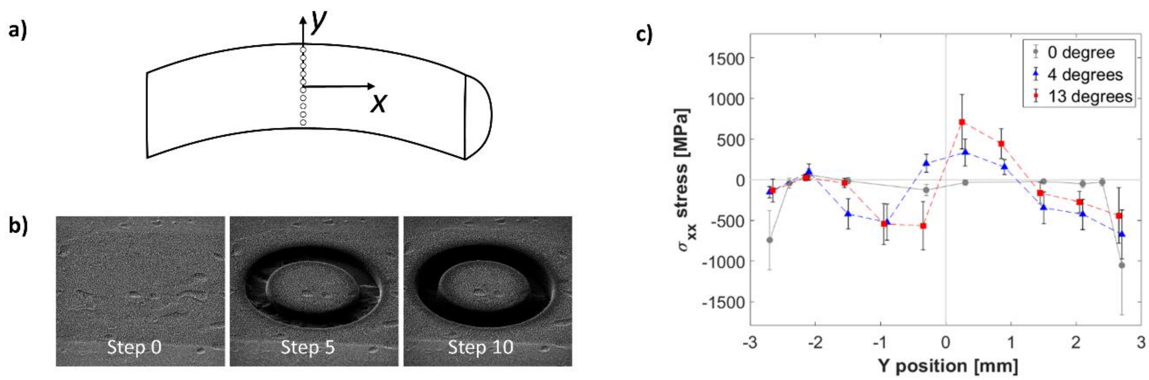

672
673 Figure 3

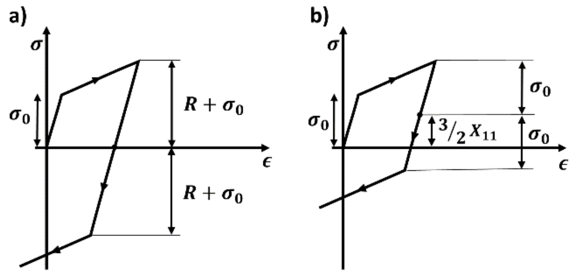
a)
b)
σ
σ_0
$R + \sigma_0$
$R + \sigma_0$
ϵ
σ
σ_0
σ_0
${}^3/_2\, X_{11}$
σ_0
ϵ

Figure 4

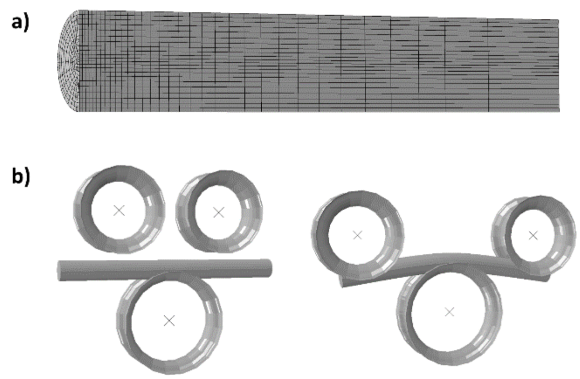

Figure 5

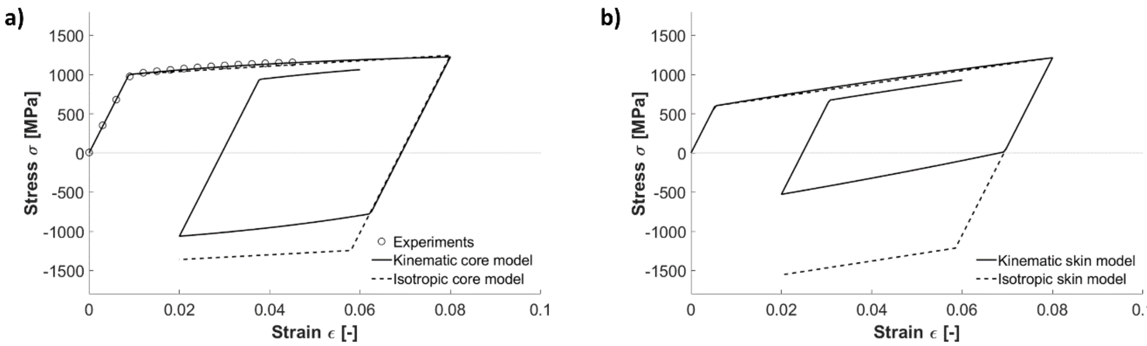
a)
Stress σ [MPa]
Strain ϵ [-]
Experiments
Kinematic core model
Isotropic core model
b)
Stress σ [MPa]
Strain ϵ [-]
Kinematic skin model
Isotropic skin model

Figure 6

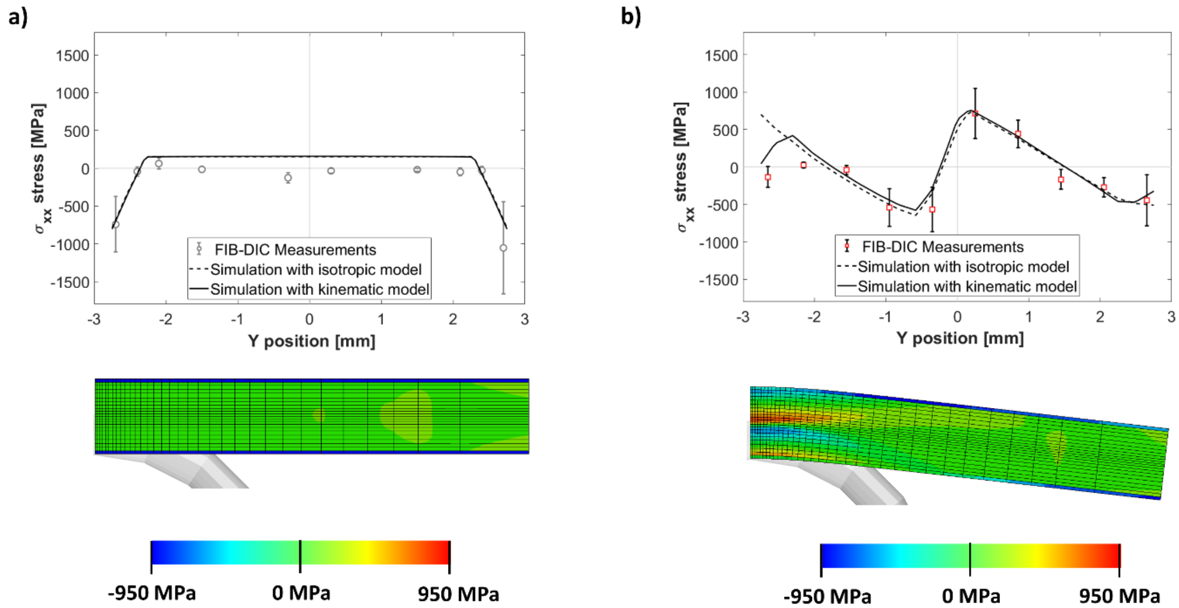
a)
b)
σ_{xx} stress [MPa]
Y position [mm]
FIB-DIC Measurements
Simulation with isotropic model
Simulation with kinematic model
-950 MPa
0 MPa
950 MPa

Figure 7

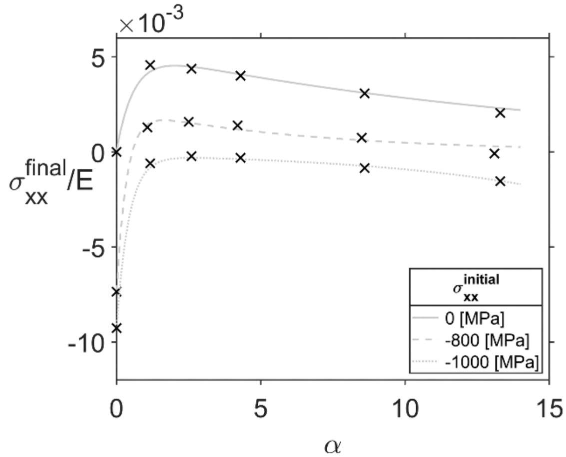
×10^-3
5
0
-5
-10
σ_xx^final/E
0
5
10
15
α
σ_xx^initial
0 [MPa]
-800 [MPa]
-1000 [MPa]

Figure 8

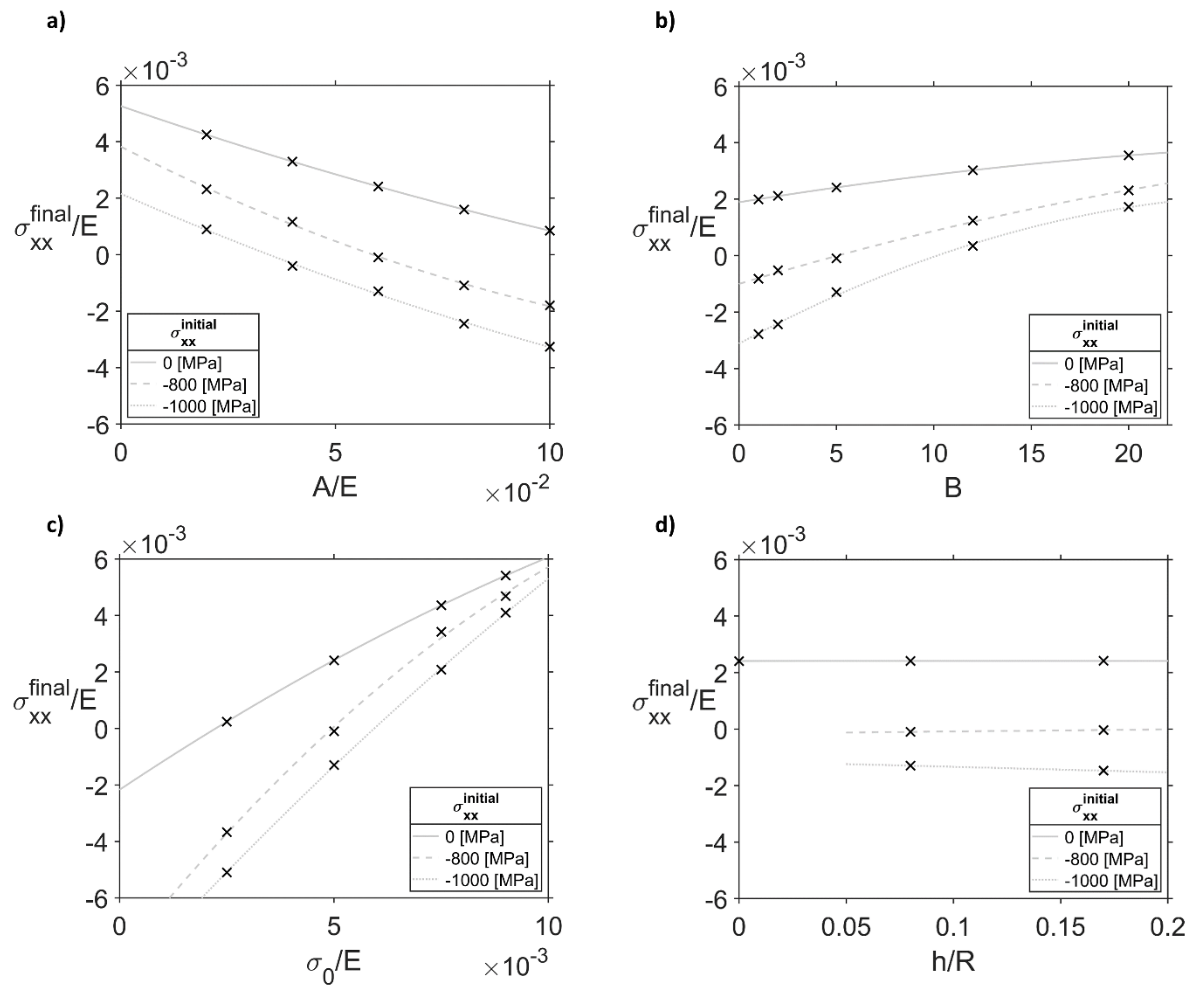
a)
b)
c)
d)
×10^-3
σ_xx^final/E
A/E
×10^-2
B
σ_0/E
×10^-3
h/R
σ_xx^initial
0 [MPa]
-800 [MPa]
-1000 [MPa]

Figure 9

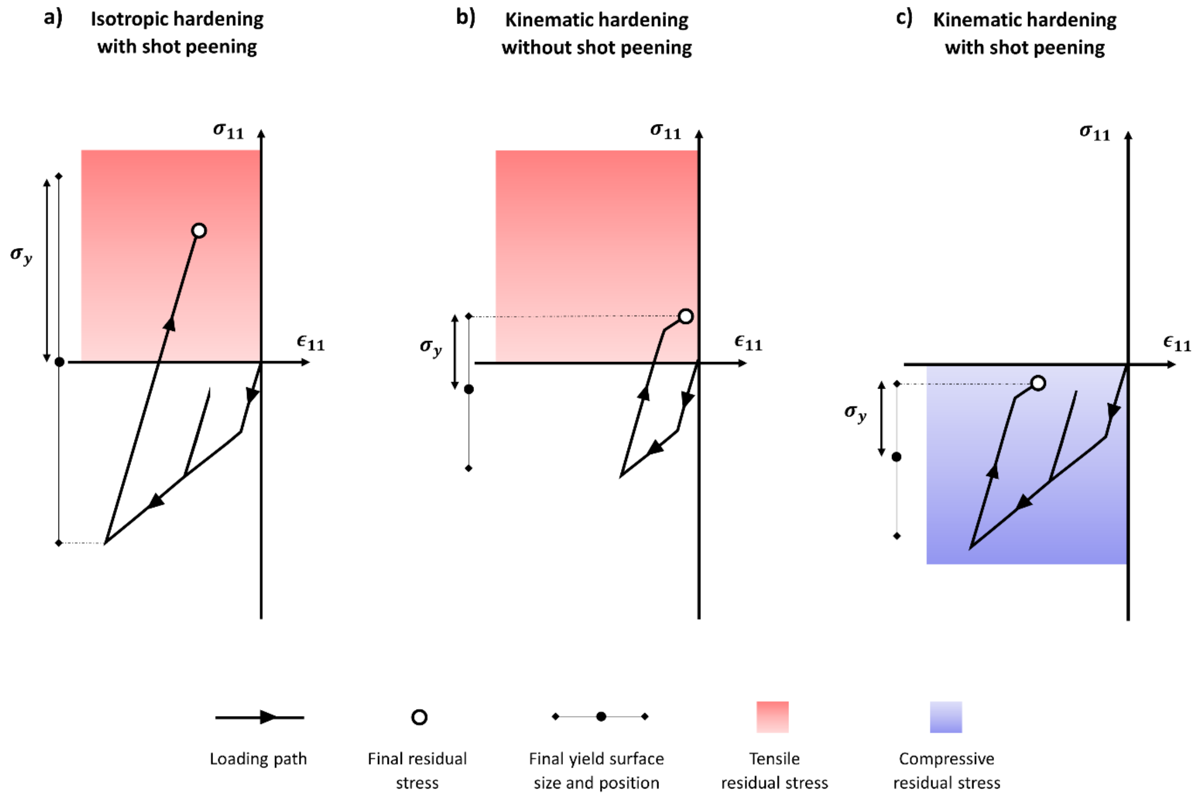
a) Isotropic hardening with shot peening
b) Kinematic hardening without shot peening
c) Kinematic hardening with shot peening
σ_{11}
ϵ_{11}
σ_y
Loading path
Final residual stress
Final yield surface size and position
Tensile residual stress
Compressive residual stress

Figure 10

	Kinematic model				Isotropic model		
Parameter	**E [MPa]**	**σ_0 [MPa]**	**A [MPa]**	**B [-]**	**E [MPa]**	**σ_0 [MPa]**	**$d\sigma/dp$ [MPa]**
Core model	113000	1000	4000	20	113000	1000	3057
Skin model	113000	600	7000	5	113000	600	8865

Table 1

Parameters	$\frac{\sigma_0}{E}$		A/E		B		$\frac{\sigma_{xx}^{initial}}{E}$	h/R
	Core	**Skin**	**Core**	**Skin**	**Core**	**Skin**		
Values	0.009	0.005	0.0035	0.06	20	5	-0.007	0.08

Table 2